Article

Mechanism of Crack Development and Strength Deterioration in Controlled Low-Strength Material in Dry Environment

Wei Peng [1] and Zili Dai [2],*

1   School of Public Affairs, Zhejiang Shuren University, Hangzhou 310015, China; 601476@zjsru.edu.cn
2   Department of Civil Engineering, Shanghai University, Shanghai 200444, China
*   Correspondence: zilidai@shu.edu.cn

Abstract: The continuous expansion at the urban scale has produced a lot of construction waste, which has created increasingly serious problems in the environmental, social, and economic realms. Reuse of this waste can address these problems and is critical for sustainable development. In recent years, construction waste has been extensively recycled and transformed into highly sustainable construction materials called controlled low-strength materials (CLSMs) in backfilling projects, pile foundation treatment, roadbed cushion layers, and other applications. However, CLSMs often experience shrinkage and cracking due to water loss influenced by climatic temperature factors, which can pose safety and stability risks in various infrastructures. The purpose of this paper was to study the mechanism of crack formation and strength degradation in a CLSM in a dry environment and to analyze the deterioration process of the CLSM at the macro- and micro-scales by using image analysis techniques and scanning electron microscopy (SEM). The test results show that with the drying time, the CLSM samples had different degrees of cracks and unconfined compressive strength (UCS) decreases, and increasing the content of ordinary Portland cement (OPC) reduced the number of cracks. The addition of bentonite with the same OPC content also slowed down the crack development and reduced the loss of UCS. The development of macroscopic cracks and UCS is caused by the microscopic scale, and the weak areas are formed due to water loss in dry environments and the decomposition of gel products, and the integrity of the microstructure is weakened, which is manifested as strength deterioration. This research provides a novel methodology for the reuse of construction waste, thereby offering a novel trajectory for the sustainable progression of construction projects.

Keywords: construction waste reuse; controlled low-strength material; dry environment; crack development; strength deterioration

1. Introduction

The ongoing urbanization process frequently involves extensive soil excavation and the generation of various solid wastes, predominantly categorized as construction waste. The disposal of this construction waste not only results in a substantial depletion of land resources and environmental pollution but also contributes to the occurrence of slope failure in landfills [1–4]. The reuse of construction waste minimizes the negative impact on the ecosystem and directly contributes to the environmental pillar of sustainable development, helping to maintain a healthy and balanced natural environment.

In recent decades, various studies have been carried out on the utilization of construction waste. For example, Priyadharshini et al. [5] investigated the possibility of utilizing

excavated soil as an alternative to river sand in a cementitious system. The results showed that it is possible to use low-plastic soil as fine aggregate by employing simple dry sieving without compromising mortar properties. Adomako et al. [6] presented a dry-washing technology for producing recycled aggregates from a mix of concrete sludge and excavation materials. Jiao et al. [7] proposed to reuse drilling waste slurry (DWS) as a grouting material for the real-time capsule grouting technique (RCG) to replace cement grouting material. Pereira et al. [8] selected excavation soils in a construction waste landfill to produce high-activity pozzolan and systematically assessed the replacement of Portland cement with calcined soils. Jiang et al. [9] used high-alumina cement (HAC) as a soil stabilization agent to modify coastal chlorine saline soil as roadbed backfilling materials. The comprehensive and in-depth research mentioned above firmly confirms that construction waste, which is generated in large quantities during demolition and construction processes, can, indeed, be recycled and transformed into a highly sustainable building material. This not only helps to reduce the environmental burden caused by the disposal of vast amounts of construction waste but also provides an economical and eco-friendly alternative for the construction industry, promoting a more sustainable development path in the long run.

Recently, construction waste has been extensively made into a sustainable construction material called controlled low-strength material (CLSM) and is widely applied across various engineering fields. For instance, Mola Abasi and Shooshpasha [10] developed a new CLSM using a blend of sand, cement, and construction waste and applied it to road construction engineering. They found that the unconfined compressive strength (UCS) and failure properties of the CLSM were improved when the cement was replaced with zeolite at an optimum proportion of 30% after 28 days. Furlan et al. [11] used dredged sediment stabilized with lime and cement as a pavement material and investigated the effect of fly ash on microstructural and resistance characteristics. Liu et al. [12] found that when calcium sulfoaluminate cement (CSA) was used to replace ordinary Portland cement (OPC) in CLSM applied to foundations, the early strength of the CLSM incorporating CSA was significantly higher than that of the CLSM using OPC. Liu et al. [13] solidified engineering excavated soils and analyzed the influence of the composition ratio of different curing agents on their strength. With its widespread application, understanding the mechanical properties of CLSM has become paramount for ensuring the safety and stability of structures and facilities, particularly in the face of climate change and extreme weather conditions [14].

Due to the impacts of climate change, including extremely high temperatures and frequent heavy rainfall, CLSM undergoes repeated cycles of drying and wetting during its service life. In arid conditions, the evaporation of moisture results in volume shrinkage and the generation of stress within the material. Shrinkage cracks form when the tensile stress surpasses the material's tensile strength [15]. According to previous research [16,17], the initiation and propagation of cracks significantly diminish the water permeability, strength, and stability of the material, rendering it more susceptible to causing the failure of slopes, riverbanks, and other constructions [18]. For example, within urban solid waste landfills, the compacted clay liner commonly experiences increased permeability due to shrinkage cracks, facilitating the migration of leachate from the waste into the groundwater through these fissures, thereby contaminating the subsurface water and environment [19,20]. On the slope, the presence of cracks compromises the overall structural integrity, creating pathways for rainwater infiltration, which can lead to slope instability and trigger landslide disasters [21]. Even the containment layer for nuclear waste in nuclear power plant waste disposal sites may experience leakage due to cracking, posing a threat to the ecological environment's safety [22–24]. The current research indicates that numerous factors such as temperature, humidity, soil composition, particle size, sample thickness, soil homogeneity, and the frequency of wet–dry cycles can influence soil cracking [25–29]. Therefore, studying

the initiation and propagation of cracks in CLSM under varying conditions is essential to ensure the stability of engineering structures.

The mechanism of soil cracking is intricate, primarily driven by changes in soil particle spacing due to water evaporation. Different patterns of soil cracking emerge under varying conditions of cyclic moisture changes, necessitating further investigation. Kishne et al. [30] examined the impact on micro-high and micro-low crack densities by assessing the soil moisture content before crack initiation. The dynamic relationship between crack density and soil moisture was accurately predicted. Specimen thicknesses also play a significant role in crack development [31–36]. Zeng et al. [31] confirmed that soil shrinkage cracking is influenced by interface friction and soil thickness under coupled interactions. Gui et al. [36] introduced a universal code for simulating soil shrinkage cracking processes across different elements, assessing the impacts of factors like shear strength, tensile strength, and soil thickness on shrinkage cracking. Moreover, reinforcing with fibers and plant root systems is deemed an effective approach to mitigate soil cracking [37–39]. Therefore, soil cracking is intricately linked to environmental factors and internal characteristics.

In this study, a controlled low-strength material (CLSM) enhanced by ultrafine bentonite is presented, and the mechanisms of crack development and strength deterioration in the CLSM in a dry environment were investigated. This experimental research focused on the cracking characteristics and strength deterioration patterns of samples with varying curing agent contents, accompanied by quantitative analysis. The results of this research are able to provide invaluable perspectives regarding the application, upkeep, and conservation of CLSMs within engineering projects, thus promoting the recycling of construction waste and diminishing its environmental footprint.

2. Materials and Methods

2.1. Experimental Material

In this study, construction waste was obtained from a construction site in Shanghai, China, and was dried, crushed, and sieved through a 2 mm sieve before the tests. Its fundamental physical properties were assessed and are presented in Table 1. The construction waste had a liquid limit of 46.7% and a plastic limit of 22.9%, classified as a low-liquid-limit clay.

Table 1. Physical characteristics of engineering excavated soil.

Water Content (%)	Liquid Limit (%)	Plastic Limit (%)	Plastic Index (/)	Density (g/cm^3)
23.5	45.5	21.7	23.8	1.81

Cement (denoted as C) and bentonite (denoted as B) were used as the primary curing agents. The cement used in this study was P.O.42.5 ordinary Portland cement (OPC), with its chemical composition displayed in Table 2. The bentonite employed was high-purity natural sodium-based bentonite, with its chemical composition presented in Table 3.

Table 2. Chemical composition of ordinary Portland cement.

Material	CaO	SiO$_2$	Al$_2$O$_3$	Fe$_2$O$_3$	SO$_3$	MgO	f-CaO
Content (%)	58.9	23.96	6.34	3.46	2.14	0.97	1.6

Table 3. Chemical composition of bentonite.

Material	CaO	SiO$_2$	Al$_2$O$_3$	Fe$_2$O$_3$	H$_2$O$^+$	H$_2$O$^-$	FeO	MgO	K$_2$O	Na$_2$O
Content (%)	1.32	54.1	18.4	1.6	4.58	12.61	0.34	2.57	0.45	1.86

2.2. Specimen Preparation

The dosage of curing agents and additives is a crucial factor affecting the curing effectiveness of soil. Cement is currently the most commonly used soil curing agent due to its high curing efficiency and low cost. In existing research related to controlled low-strength materials (CLSMs), the dosage of the cement typically ranged from 5% to 20% [40,41]. Bentonite, known for its strong expansiveness and hygroscopic properties, can significantly improve the engineering characteristics of cement paste, such as viscosity and water absorption. However, the workability of the mixture decreases considerably by increasing the bentonite dosage. Previous studies have shown that the improvement is most pronounced when the bentonite dosage is around 6% [42]. Therefore, the dosages of cement and bentonite were determined to be f_c = 5%, 10%, 15%, and 20% and f_b = 0% and 6% in this research, as shown in Table 4. When preparing the samples, the dry materials, which contained the clayey soil, cement, and bentonite, were mixed according to the mix proportions and quickly stirred with a motor agitator for 10 min. Then, a specific dose of water was gradually added to the dry mixtures and blended for another 10 min. This method has been proven to be effective in obtaining homogeneous slurries in previous research [43].

Table 4. The cement and bentonite dosages of the specimens in the experiments.

Specimen Number	Cement (%)	Bentonite (%)
C1	5	0
C2	10	0
C3	15	0
C4	20	0
BC1	5	6
BC2	10	6
BC3	15	6
BC4	20	6

In the experiment, the dosage of the curing agent, OPC, was calculated as

$$f_c = \frac{m_c}{m_s}, \tag{1}$$

where f_c (%) is defined as the dosage of the curing agent, OPC, m_c (g) is the mass of the OPC, and m_s (g) is defined as the mass of the soil specimen.

The dosage of bentonite was calculated as

$$f_b = \frac{m_b}{m_w}, \tag{2}$$

where f_b (%) is defined as the bentonite dosage, m_b (g) is the mass of the bentonite, and m_w (g) is defined as the mass of the water used.

Prior to the CLSM's preparation, a cylindrical mold with an inner diameter of 80 mm and a height of 80 mm was employed to control the flowability of the samples to 116 ± 2 mm. In the UCS tests, a mold with dimensions of 70 mm × 70 mm was used, while a mold with a diameter of 90 mm and a height of 20 mm was utilized for the drying tests. According to the experimental protocol, a thin layer of petroleum jelly was evenly

applied to the inner walls of the mold to minimize friction between the sample and the mold as much as possible. After adding an appropriate amount of water to adjust the flowability of the mixture, the homogeneous mixture was poured into the mold and thoroughly compacted to achieve the desired density while precisely controlling the sample height to ensure uniformity. The surface of each sample was then leveled off before being placed in a standard curing room for a period of 7 days.

2.3. Experimental Device and Method

In this work, the unconfined compressive strength (UCS) of the specimens was tested using a Microcomputer Control Electronic Universal Testing Machine (CTM8050, Shanghai Xieqiang Instrument Co., Ltd., Shanghai, China). The measurement range was 0–50 kN with an accuracy of ±0.01%. The drying test was carried out by an ICH110 Climate Chamber with a setting temperature range of −10 to +60 °C and a resolution of 0.1 °C. Scanning electron microscopy (SEM) was utilized to investigate the morphological characteristics of the CLSM. The resolution was 0.6 nm@15 kV, with WD = 5 mm. All the experiments in this research were conducted according to the standard for geotechnical testing method (GB/T 50123-2019) [44].

After the CLSM samples reached the specified curing duration, they were removed from the curing room. For the samples designated for UCS testing, one group was subjected to immediate strength testing, while another group was placed in a drying oven for continuous drying. According to Zeng et al. [45], a temperature of 30 °C is suitable for the experimental investigation of soil-cracking mechanisms. Therefore, the temperature of the oven in the drying test was controlled at 30 °C. The weight of each sample was measured every two hours, and testing was conducted when the weight difference between two consecutive measurements was minimal. The samples intended for drying testing were placed in a testing apparatus set at a temperature of 30 °C, with mass changes recorded every two hours. Simultaneously, a camera was positioned above the samples to document any surface crack developments. The final data for moisture loss were recorded when the weight difference between consecutive measurements was minimal. The flow chart of the test methods is shown in Figure 1.
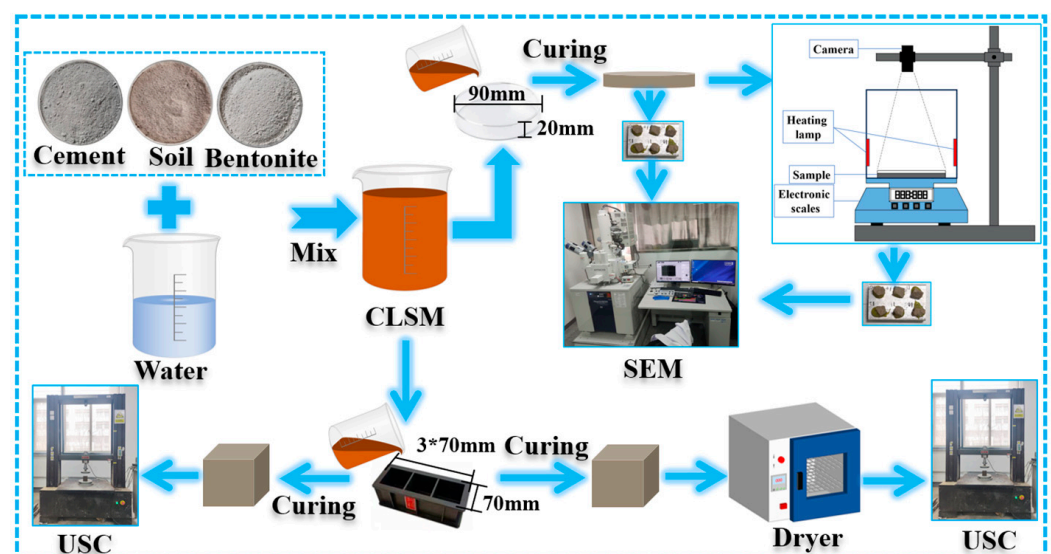

Figure 1. Flow chart of test methods.

In a dry environment, the water in a CLSM specimen absorbs the heat from the atmosphere and evaporates into the environment, thereby reducing the soil quality. Water molecules in the specimen are presented in two states: free water and bound water. Discrep-

ancies in the initial water–cement ratios can result in varying moisture levels in specimens at the start of drying tests. Hence, the water loss rate (*W*) serves as a metric to describe the rate of moisture depletion from the specimens:

$$W = \frac{m_i - m_0}{m_0},$$ (3)

where *W* is the cumulative water loss rate of the specimen, m_i is the weight of the specimen at time *i*, and m_0 is the initial weight of the specimen at the beginning of the drying process.

2.4. Crack Image Processing

To quantitatively analyze the progression of surface cracks during desiccation, the specimen's surface image in Figure 2a was imported into Photoshop and converted to grayscale, as shown in Figure 2b. Subsequently, the grayscale image was binarized to obtain Figure 2c, and then the noise affecting the surface calculations was eliminated, as shown in Figure 2d. Using Image-Pro Plus 6.0, the processed Photoshop image (Figure 3) was utilized to quantify the total crack length on the specimen surface, the surface crack ratio (the total crack area-to-specimen area ratio), the maximum crack width (the widest single crack on the specimen surface), and the average crack width (the ratio of the crack area to the total crack length on the specimen surface). By comparing the pixel width of the specimen image with the specimen diameter, the relevant crack parameters were calculated. The specific conversion process is outlined as follows.

$$L = \mu P,$$ (4)

where *L* is the specimen diameter, *μ* is the conversion factor, and *P* is the pixel width of the specimen image.
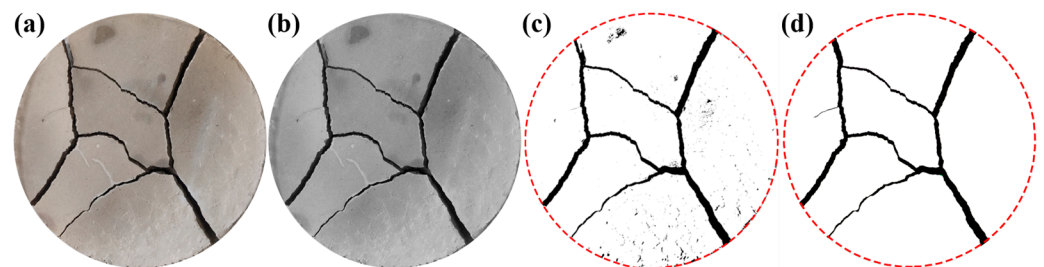

Figure 2. Image-processing process: (**a**) original crack image, (**b**) grayscale image, (**c**) image of crack after binarization, and (**d**) binarized image after removing spurious points.
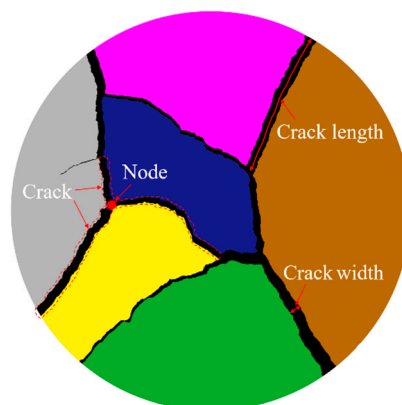

Figure 3. Crack identification schematic diagram.

3. Experimental Results

3.1. Water Evaporation Law of Specimens

The water loss rate and evaporation rate curves over time for two CLSM specimens with varying dosages of the curing agent are depicted in Figure 4. The results reveal distinctions in the water evaporation behavior of the CLSM specimens compared with conventional saturated soil. According to Tang et al. [26], the evaporation rate history of saturated soil evolves through three stages as the drying time advances: the normal rate evaporation phase (NRE), the deceleration rate evaporation phase (DRE), and the residual rate evaporation phase (RRE), as shown in Figure 4a. Initially, during the evaporation of the CLSM specimens, the rate increased with the drying time, indicating the accelerated rate evaporation phase (ARE), as illustrated in Figure 4b, where the curve's slope gradually rises with the drying time. Upon transitioning to the NRE phase, the water loss rate demonstrates a nearly linear growth trend, maintaining a relatively constant water evaporation rate for the specimen. Progressing to the DRE phase, the slope of the water loss rate curve gradually diminishes with the prolonged drying time, leading to a gradual reduction in the specimen's water evaporation rate. Finally, the water evaporation rate gradually reaches stability with the increasing drying time, progressing to the RRE phase.
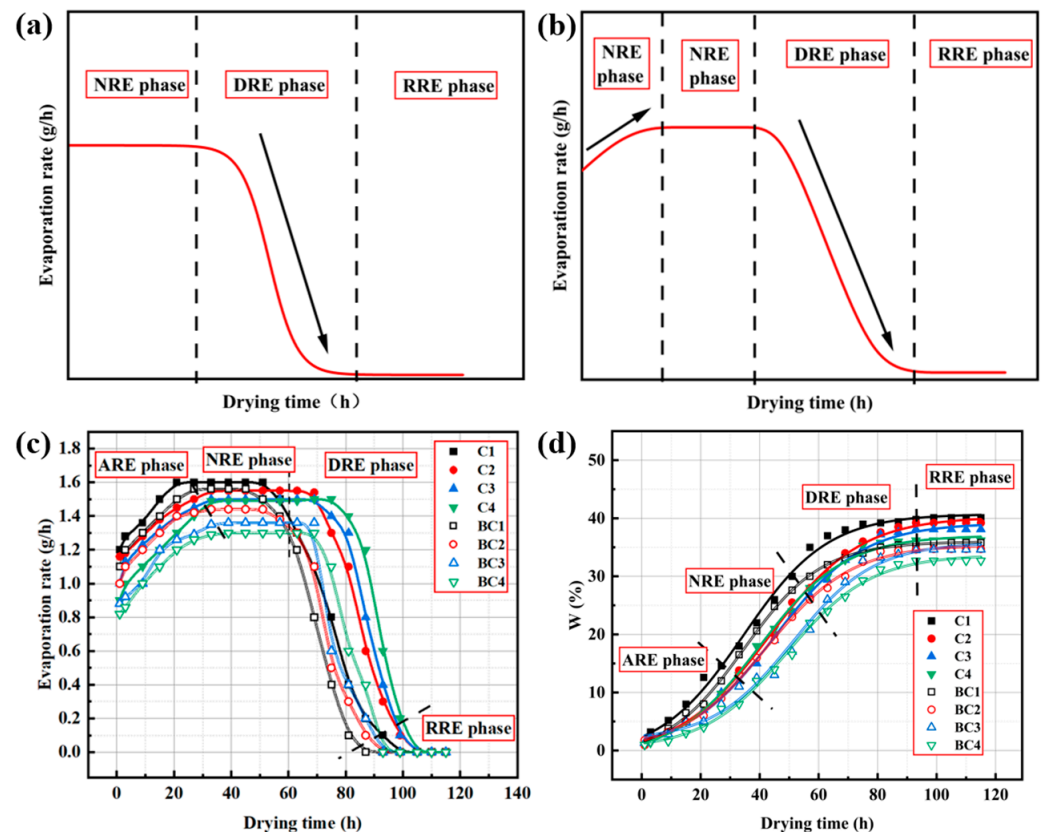

Figure 4. Curves of water evaporation law of two CLSM specimens: (**a**) three phases of evaporation rate change in saturated soils [26], (**b**) four phases of evaporation rate change in CLSM, (**c**) evaporation rate curves for two CLSM specimens, and (**d**) water loss rate curves for two CLSM specimens.

Comparing the curves of the evaporation rate over the drying time for the two different types of CLSM specimens in Figure 4c, for the same OPC content, the CLSM specimens with bentonite had a significantly lower evaporation rate compared with those without bentonite, and the time taken for water evaporation was shorter. When increasing the OPC content, the water evaporation rate of both types of CLSM specimens decreased. Comparing the curves of the water loss rate over the drying time for the two different types

of CLSM specimens in Figure 4d, it is evident that for the same OPC content, the CLSM specimen with bentonite had a lower final water loss rate compared with those without bentonite. As the OPC content increased, the final water loss rate of both types of CLSM specimens decreased.

Based on the experimental results, the time–moisture loss data for the two types of CLSM could be effectively modeled using the Boltzmann function. The fitting function expression is as follows:

$$\omega = A2 + \frac{A1 - A2}{1 + e^{(t-t_0)/dt}},$$ (5)

where ω is the moisture loss rate of the specimen, t is the time, and A1, A2, and t_0 are three fitting parameters.

The Boltzmann fitting results are shown in Table 5, where a value of R_2 closer to 1 indicates a smaller error. It can be observed that the cumulative moisture loss curve data fitted by the Boltzmann function closely align with the original experimental data in the starting, ending, and transition sections.

Table 5. Boltzmann function fitting degrees.

Sample	C1	C2	C3	C4	CB1	CB2	CB3	CB4
R^2	0.998	0.997	0.997	0.998	0.998	0.988	0.993	0.997

3.2. Crack Development Process in CLSM

Comparing the specimen images with the varying curing agent dosages in Figure 5, significant differences in the crack morphologies on the specimen surfaces can be noted with the varying OPC dosages. Specimen C1, treated with a lower curing agent dosage, displayed dense and intersecting cracks with significant lengths and small average widths. Likewise, specimens C1–C4 and BC1–BC2 all exhibited complete failure, causing the cured soil specimens to fracture into irregular quadrilateral or pentagonal blocks after water loss. In the specimens treated with a high curing agent dosage, the surface cracks appeared more pronounced and were significantly influenced by boundary effects (e.g., C4), resulting in larger total crack lengths and wider average widths for the segmented soil blocks and cracks. Illustrated in Figure 5, the surface cracks initially exhibited elongation and narrowness. Subsequently, with a slight rise in the cumulative water loss rate, the crack length underwent rapid development while retaining a narrow width, forming the primary crack morphology of the specimen. The increase in the cumulative water loss rate of the sample led to the expansion of the crack width, and the specimen was divided into CLSM blocks of different sizes.

After the drying test, the cracks on the specimen surfaces exhibited two forms at the intersections: a "T" shape and a "Y" shape (as shown in Figure 6). The cured soil samples were divided into quadrilaterals or pentagons. After the addition of bentonite, there was no apparent change in the crack node morphology and soil block morphology.
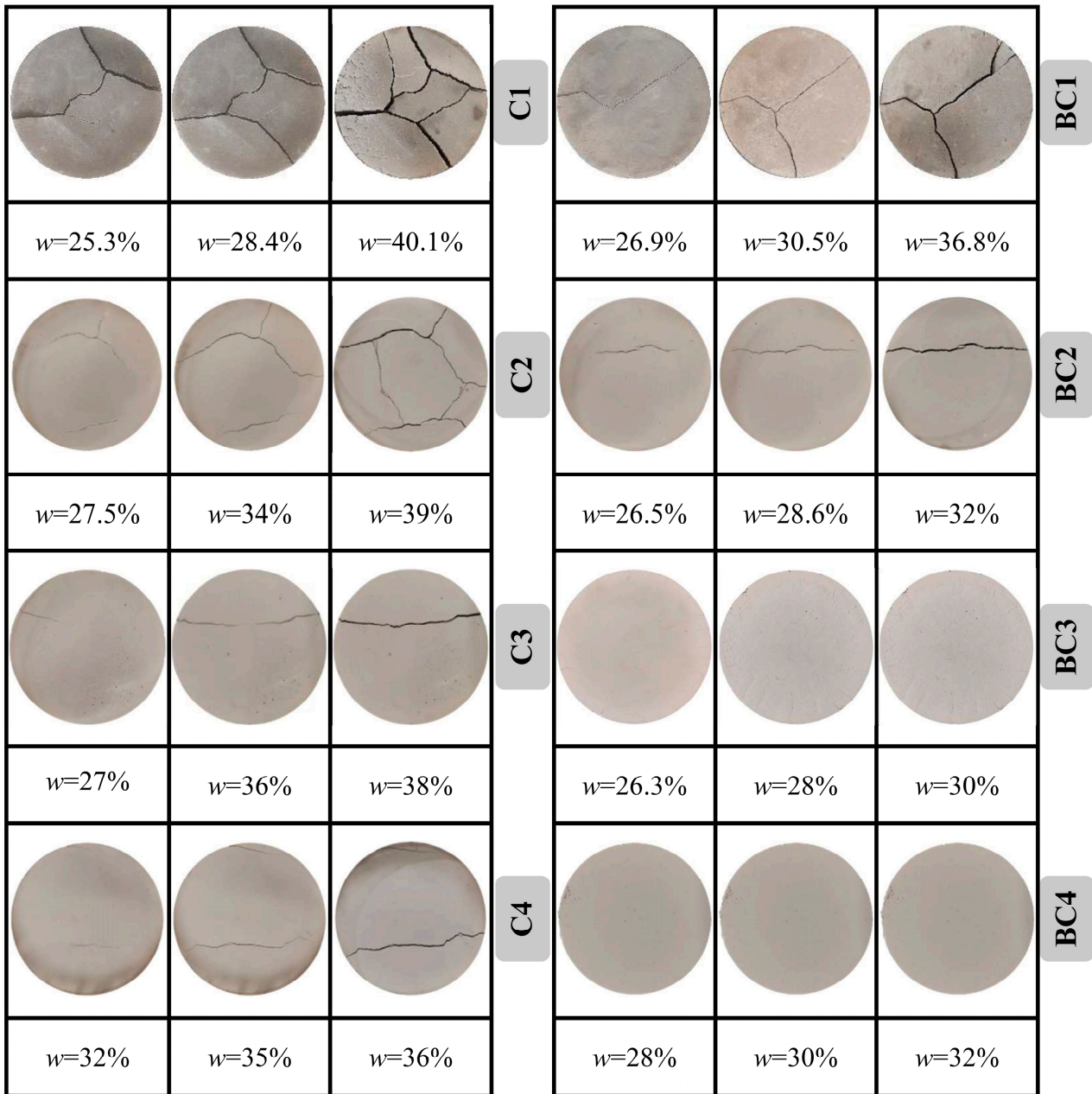
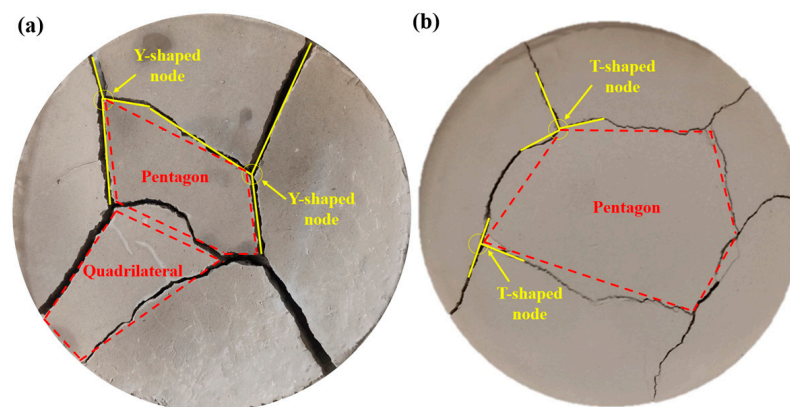**Figure 5.** Relationship between surface crack evolution process and moisture loss rate.

Figure 6. Schematic diagram of CLSM fracture and soil clod morphology: (**a**) Y-shaped crack and (**b**) T-shaped crack.

3.3. Influence of OPC and Bentonite Dosages on Crack Morphology

This study extracted and quantitatively analyzed the crack images of the specimens observed during the drying tests, identifying key crack indicators, such as the crack ratio, average crack width, and total crack length. Figure 7 depicts the quantitative descriptors of the crack morphology in the final stage of drying for the two types of CLSM when varying the dosages of the curing agent. As shown in Figure 7a, the surface crack ratios in the final drying stage for specimens C1, C2, C3, and C4 were 6.65%, 1.82%, 1.47%, and 0.95%, respectively. Compared with C1, the surface crack ratios for C2, C3, and C4 decreased by 72.6%, 77.9%, and 85.7%, respectively. Similarly, the surface crack ratios in the final drying stage for specimens BC1, BC2, BC3, and BC4 were 2.52%, 1.38%, 0.15%, and 0%, respectively. Compared with BC1, the surface crack ratios for BC2, BC3, and BC4 decreased by 45.2%, 94.0%, and 100.0%, respectively. The surface crack ratios of both types of CLSM decreased consistently as the dosage of the curing agent increased, with reduction rates of up to 100%. This phenomenon can be attributed to the fact that the tensile strength of CLSM specimens is determined by the cohesion force between particles, which is influenced by capillary forces arising from water bridges or bodies between the soil particles.
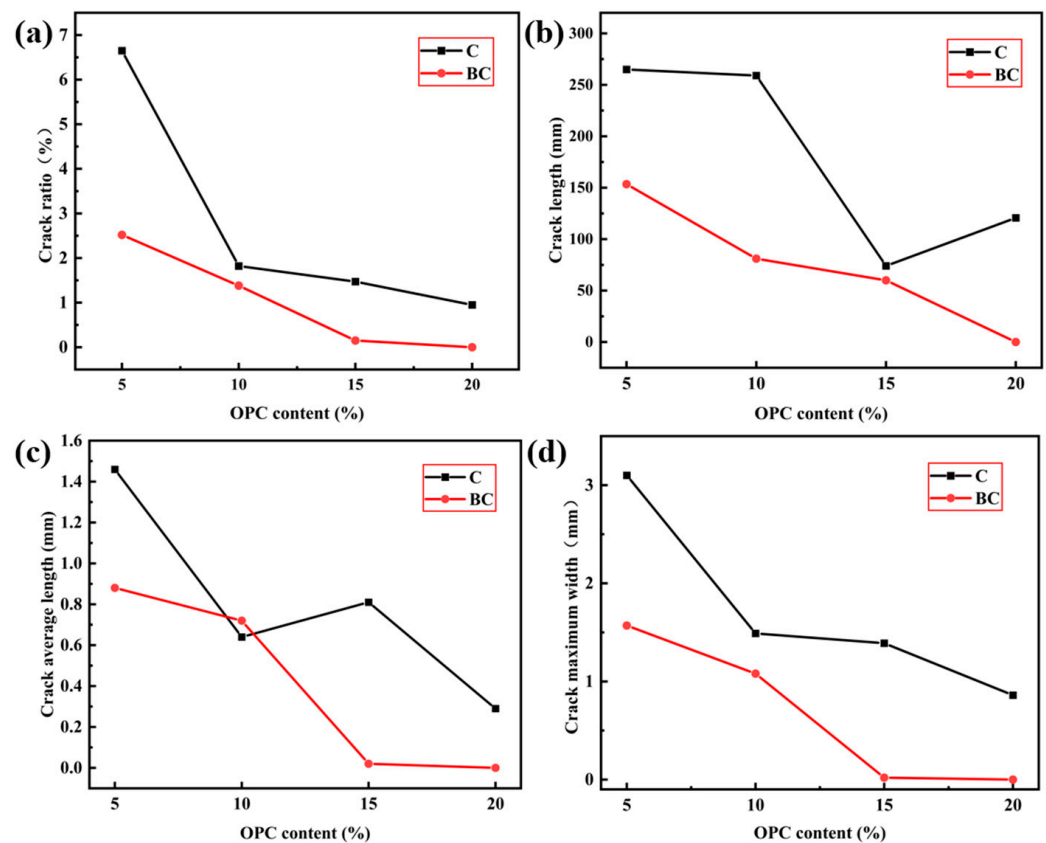

Figure 7. The quantitative indicators of final-stage cracks in two types of CLSM as amount of solidifying agent varied: (**a**) relationship between sample crack ratio and OPC content, (**b**) relationship between sample crack length and OPC content, (**c**) relationship between average length of cracks in samples and OPC content, and (**d**) relationship between maximum width of cracks in samples and OPC content.

With an increase in the curing agent dosage, the gel and aggregates produced filled the voids between soil particles, thereby decreasing the soil porosity, increasing the number of effective contact points between aggregates and particles, and, consequently, enhancing the soil's tensile strength. The addition of bentonite led to a reduction in the surface crack ratios of specimens BC1, BC2, BC3, and BC4 compared with C1, C2, C3, and C4 by 62.1%, 24.2%,

89.8%, and 100%, respectively. These findings suggest that incorporating bentonite at the same cement dosage can effectively reduce the surface crack ratios of CLSM specimens. During the experiment, the bentonite absorbed the water and then expanded, filling the voids between particles in the CLSM, thereby reducing the void volume, increasing the aggregate contact points, and improving the tensile strength. Additionally, the components in the bentonite reacted with the cement hydration products to form aggregates, further enhancing the soil tensile strength as the quantity of aggregates increased. Figure 7b illustrates a decrease in the total crack lengths of both types of CLSM with an increase in the curing agent dosage. The addition of bentonite at the same cement dosage resulted in reduced total crack lengths of the specimens, particularly notable at the 10% and 20% cement dosages, with reductions of 68.7% and 100%, respectively. As depicted in Figure 7c, the crack widths of specimens C1, C2, C3, and C4 in the final drying stage were 1.6 mm, 0.62 mm, 0.75 mm, and 0.35 mm, respectively, decreasing as the cement dosage increased. Conversely, specimens BC1, BC2, BC3, and BC4 exhibited crack widths of 0.97 mm, 0.75 mm, 0.10 mm, and 0.00 mm, respectively, in the final drying stage, showing an inverse relationship with the cement dosage. Bentonite had a more pronounced impact on the crack width of the CLSM specimens when the cement dosage surpassed 15%. The maximum crack width serves as an indicator of the overall degree of fragmentation of a CLSM. Smaller maximum crack widths indicate more-intact CLSM specimens, leading to enhanced mechanical and anti-seepage properties after dehydration. As shown in Figure 7d, the maximum crack widths of specimens C1, C2, C3, and C4 in the final drying stage were 3.1 mm, 1.49 mm, 1.39 mm, and 0.86 mm, respectively, while specimens BC1, BC2, BC3, and BC4 exhibited maximum crack widths of 1.57 mm, 1.08 mm, 0.02 mm, and 0.00 mm, respectively. The maximum crack widths of both types of CLSM exhibited a negative correlation with the cement dosage, with the impact of adding bentonite becoming notably significant when the cement dosage exceeded 15%.

3.4. Variation in Strength After Drying

Figure 8 illustrates the stress–strain curves of the UCS test before and after drying for the two types of CLSM samples after 7 days of curing. The test results show that after drying and water loss, the strains of the samples without bentonite decreased from 2.6%, 3.7%, 4.4%, and 4.9% to 1.1%, 1.3%, 1.8%, and 2.7%, respectively, when the stress reached its peak. The strains of the bentonite-added samples decreased from 4.3%, 5.8%, 7.6%, and 8.5% to 2.6%, 3.6%, 4.2%, and 6.1%, respectively, when the stress reached its peak. The strains corresponding to the peak stress values of the two CLSM samples after drying and water loss were smaller, the brittleness increased, and brittle ring-breaking characteristics appeared. When the cement content was the same, the ductility after drying and water loss could be increased by adding bentonite, and the risk of brittle failure could be reduced. At the same time, the residual strength of the two CLSM samples decreased to varying degrees after drying and water loss, and the residual strength of the samples could be increased by adding gel materials. By analyzing the peak values of the stress–strain curves in Figure 8, the addition of bentonite improved the unconfined compressive strength of the CLSM sample when the cement content was the same.

The curves in Figure 9 depict the unconfined compressive strength reduction rates of the two types of CLSM samples after drying water loss to better distinguish the strength variations in the samples before and after drying and the relationship between the strength change and the gel material content. The strength reduction rate was used to evaluate the mechanical properties of the CLSM samples in a dry environment. The D_r was calculated using Equation (5):

$$D_r = \frac{S_0 - S_d}{S_0} \tag{6}$$

where D_r represents the reduction rate of the unconfined compressive strength of the sample, S_0 indicates the strength of the sample that has not been dried, and S_d represents the strength of the sample after drying and water loss.
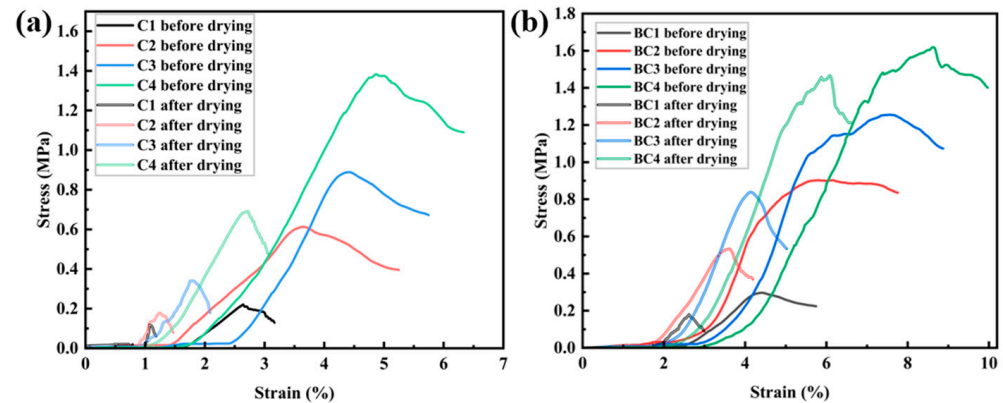
Figure 8. Stress–strain relationship of samples recorded before and after drying: (**a**) no-bentonite-added CLSM; (**b**) bentonite-added CLSM.
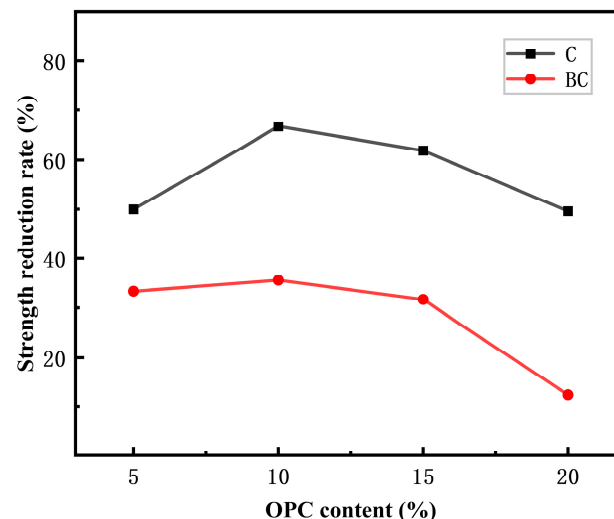
Figure 9. Strength reduction rates of CLSM samples after drying.

The results in Figure 9 show that the addition of bentonite could significantly reduce the strength loss of the CLSM after water loss in a dry environment, and the effect of the bentonite was more obvious with the increase in the cement content. When the cement content was greater than 10%, the strength loss of the two CLSM samples decreased with the increase in the OPC content. In a dry environment, the content of OPC can be increased appropriately, and gel materials, such as bentonite, can be added to reduce the strength loss and reduce the possibility of brittle failure.

4. Discussion

4.1. Mechanism of CLSM Microstructure

The microstructural principle of CLSMs is that OPC hydration produces various hydration products, which effectively combine soil particles to form a spatial network structure. The main product of the OPC hydration reaction is calcium–silicate–hydrate

(C-S-H) gels, which exist in CLSMs in the form of reticules, colloids, or flocculants, and the network structure formed by their combination with soil particles is the main source of CLSMs' strength [46,47]. Ettringite in OPC products is critical for the early strength and durability performance of CLSMs.

Montmorillonite particles typically exhibit a positive charge on their edges, while the particle surface carries a negative charge. The magnitude of the negative charge on the particle surface surpasses the positive charge on the particle edges, resulting in mutual attraction between the particles [48]. Conversely, OPC particles, which predominantly bear positive charges on their surfaces, outnumber montmorillonite particles. The interaction between OPC and bentonite particles on the particle surface facilitates the dispersion of bentonite particles in the cement slurry, underscoring the importance of maintaining an appropriate bentonite content in the sample. Excessive bentonite particles can aggregate and impede water absorption, hindering adequate contact and reaction with OPC. During the induction period, the calcium hydroxide content in the hydration products reaches supersaturation. Silica and alumina in bentonite react with calcium hydroxide to produce insoluble, stable hydration products, contributing to the densification of the microstructure of the CLSM. Montmorillonite particles primarily serve to fill voids and enhance the microstructure of CLSMs. The reactivity between montmorillonite and OPC is relatively limited compared with the hydration process.

Figure 10 depicts the scanning electron microscope (SEM) images of the CLSM specimens with varying curing agent dosages, magnified 2000 times. In Figure 10a, when the OPC dosage is low, minimal amounts of C-S-H gel and needle-like AFt are visible on the surfaces of the soil particles, exhibiting high porosity and compromised integrity. This observation correlates with the reduced crack resistance of the CLSM specimen in the drying tests. Furthermore, the pronounced porosity at the microstructural level accelerated water loss and promoted rapid crack formation. With an increase in the OPC dosage, as illustrated in Figure 10b, hydration products experienced a substantial rise, diminishing the specimen's porosity while bolstering its structural integrity and the overall cohesion between particles. The introduction of bentonite as an additive, as depicted in Figure 10c, triggered a reaction between OPC hydration products and components in the bentonite, generating gels and aggregates and leveraging the filling properties of montmorillonite. This transformative process densified the CLSM structure, enhancing its overall integrity and crack resistance, aligning with the improved water dispersion inhibition performance observed in specimens with an identical curing agent dosage but incorporating bentonite in the experiment.
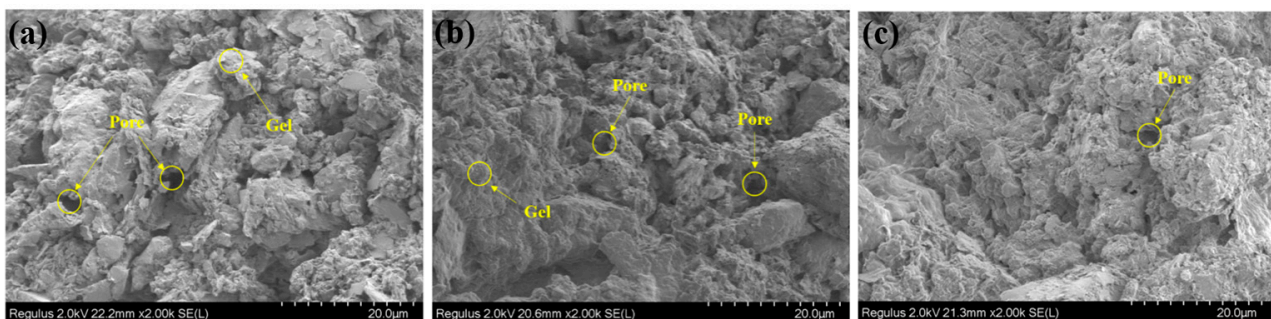

Figure 10. SEM images of samples with varying OPC contents: (**a**) OPC content of 5%, (**b**) OPC content of 15%, and (**c**) OPC content of 15% + bentonite.

4.2. Microscopic Deterioration Mechanism of CLSM

The cracking of CLSM is affected by many factors, but, in general, its surface tensile stress and material tensile strength are the key factors that determine the crack behavior [49]. Tensile failure is the main form of material cracking, and cracks appear when the tensile stress on the surface is greater than the tensile strength of the material. Studies have shown that the tensile strength of CLSM comes from the cementation of soil particles and the filling of pores between soil particles by the hydration products of the curing agent [50].

Figures 11 and 12 are SEM images of the CLSM samples with the same gel material content before and after drying, respectively. In the drying test, the continuous loss of moisture inside the CLSM sample caused carbon dioxide in the air to enter the sample through the pores, react with $Ca(OH)_2$, reduce the pH value inside the sample, and cause the hydration products of the cementitious material to decompose into calcium carbonate, gypsum, and aluminum glue [51], and the gel of the cemented soil particles inside the sample was consumed, and the microstructure became loose, the integrity was weakened, and the strength was reduced. This resulted in weak areas inside the sample, and when the stress from the uneven dry shrinkage was greater than the tensile stress of the sample, the sample surface was damaged, and cracks were created. After adding bentonite to the CLSM, the main components of bentonite and $Ca(OH)_2$ in the sample reacted to form amorphous hydrated calcium silicate, which reduced the decomposition of the C-S-H gel in a dry environment, inhibited the appearance of cracks after water loss, and slowed down the loss of strength.
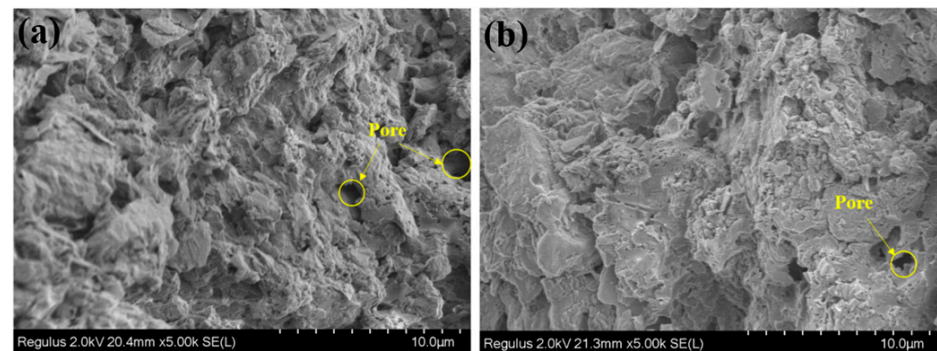

Figure 11. SEM images of samples before the drying experiment: (**a**) OPC content of 10% + bentonite; (**b**) OPC content of 20% + bentonite.
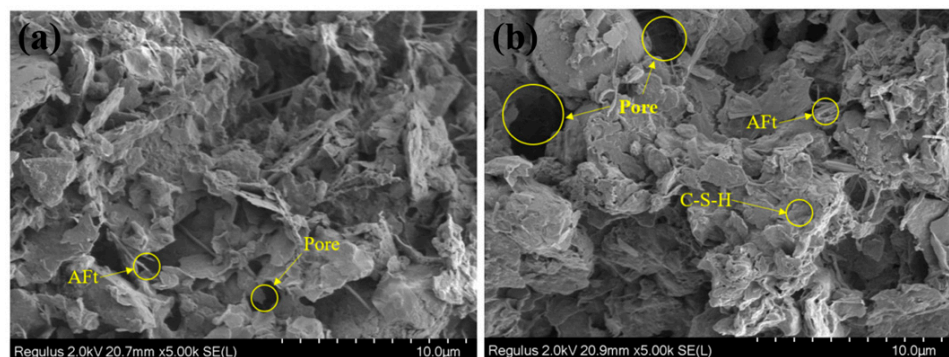

Figure 12. SEM images of samples after the drying experiment: (**a**) OPC content of 10% + bentonite; (**b**) OPC content of 20% + bentonite.

5. Conclusions

With the continuous expansion at the urban scale, engineering excavated soils produced in the construction process have been extensively made into controlled low-strength materials and adopted in various fields, such as roadbeds, grouting materials, and foundation backfill. In this paper, the crack development and strength deterioration mechanism of a CLSM in a dry environment were studied, and the water dispersion loss law of the CLSM was analyzed by comparing the characteristics of the water loss rate with time and the crack rate with the water loss rate of samples with different gel material contents during the drying test process, and the crack images were processed by digital image technology to analyze the crack development law. The drying test was used to analyze the variations in the CLSM's strength in a dry environment. In addition, the structural mechanism of the CLSM and the microstructural change law after the drying test were analyzed at the microscopic level, and the following results were obtained:

(1) In dry conditions, the surface of the CLSM exhibited varying degrees of cracking, leading to the degradation of the soil strength. Appropriately increasing the cement content and incorporating bentonite could enhance both the strength and durability of the CLSM, resulting in a significant improvement in its performance.

(2) The hydration products of OPC were the primary source of strength in the CLSM. The optimal content of OPC was found to be 15%, at which point the specimen incorporating bentonite did not exhibit any significant surface cracks at the end of the experiment.

(3) Bentonite primarily enhanced the microstructure of the CLSM through its expansion and filling effects, resulting in the increased integrity of the specimens and improved crack resistance.

To reveal the chemical reaction mechanism of bentonite and cement, X-ray diffraction (XRD) analysis should be included to specify how bentonite affects the chemical properties and phase structure. In addition, future research could consider the incorporation of new types of fiber materials that significantly enhance the tensile properties of CLSMs to further improve their crack resistance.

Institutional Review Board Statement: Not applicable.

Informed Consent Statement: Not applicable.

Data Availability Statement: The data presented in this study are available upon request from the corresponding author.

Conflicts of Interest: The authors declare no conflicts of interest.

References

1. Duan, H.; Wang, J.; Huang, Q. Encouraging the environmentally sound management of C&D waste in China: An integrative review and research agenda. *Renew. Sustain. Energy Rev.* **2015**, *43*, 611–620.

2. Duan, H.; Miller, T.R.; Liu, G.; Tam, V.W. Construction debris becomes growing concern of growing cities. *Waste Manag.* **2019**, *83*, 1–5. [CrossRef]

3. Qin, X.Q.; Huang, Y.J.; Wang, C.S.; Jiang, K.B.; Xie, L.F.; Liu, R.; Shi, X.G.; Chen, X.S.; Zhang, B.C. A temporary soil dump settlement and landslide risk analysis using the improved small baseline subset-InSAR and continuous medium model. *Int. J. Appl. Earth Obs. Geoinf.* **2024**, *128*, 103760. [CrossRef]

4. Yin, Y.; Li, B.; Wang, W.; Zhan, L.; Xue, Q.; Gao, Y.; Zhang, N.; Chen, H.; Liu, T.; Li, A. Mechanism of the December 2015 catastrophic landslide at the Shenzhen landfill and controlling geotechnical risks of urbanization. *Engineering* **2016**, *2*, 230–249. [CrossRef]

5. Priyadharshini, P.; Ramamurthy, K.; Robinson, R.G. Reuse potential of stabilized excavation soil as fine aggregate in cement mortar. *Constr. Build. Mater.* **2018**, *192*, 141–152. [CrossRef]

6. Adomako, S.; Engelsen, C.J.; Døssland, L.T.; Danner, T.; Thorstensen, R.T. Technical and environmental properties of recycled aggregates produced from concrete sludge and excavation materials. *Case Stud. Constr. Mater.* **2023**, *19*, e02498. [CrossRef]

7. Jiao, C.; Diao, Y.; Zheng, G.; Liu, Y.; Huang, J.; Zhang, Y.; Zhao, L. Reuse of Drilling Waste Slurry as the Grouting Material for the Real-Time Capsule Grouting Technique. *Materials* **2023**, *16*, 1540. [CrossRef]

8. Pereira, V.M.; Baldusco, R.; Nobre, T.; Quarcioni, V.A.; Coelho, A.C.; Angulo, S.C. High activity pozzolan obtained from selection of excavation soils in a Construction and Demolition Waste Landfill. *J. Build. Eng.* **2024**, *84*, 108494. [CrossRef]

9. Jiang, Y.; Dai, H.; Fisonga, M.; Li, C.; Hong, Z.S.; Xia, C.; Deng, Y.F. Feasibility and mechanism of high alumina cement-modified chlorine saline soil as subgrade material. *Constr. Build. Mater.* **2024**, *429*, 136411. [CrossRef]

10. Mola Abasi, H.; Shooshpasha, I. Influence of zeolite and cement additions on mechanical behavior of sandy soil. *J. Rock Mech. Geotech. Eng.* **2016**, *8*, 746–752. [CrossRef]

11. Furlan, A.P.; Razakamanantsoa, A.; Ranaivomanana, H.; Amiri, O.; Levacher, D.; Deneele, D. Effect of fly ash on microstructural and resistance characteristics of dredged sediment stabilized with lime and cement. *Constr. Build. Mater.* **2021**, *272*, 121637. [CrossRef]

12. Liu, H.; Zhao, J.; Wang, Y.; Yi, N.; Cui, C. Strength performance and microstructure of calcium sulfoaluminate cement-stabilized soft soil. *Sustainability* **2021**, *13*, 2295. [CrossRef]

13. Liu, S.; Zhan, J.; Wang, X. Influence of composition of curing agent and sand ratio of engineering excavated soil on mechanical properties of fluidized solidified soil. *Mater. Sci.-Pol.* **2023**, *41*, 57–67. [CrossRef]

14. Qian, J.S.; Hu, Y.Y.; Zhang, J.K.; Xiao, W.X.; Ling, J.M. Evaluation the performance of controlled low strength material made of excess excavated soil. *J. Clean. Prod.* **2019**, *214*, 79–88. [CrossRef]

15. Gao, Q.F.; Yu, H.; Zeng, L.; Zhang, R.; Zhang, Y.H. Roles of vetiver roots in desiccation cracking and tensile strengths of near-surface lateritic soil. *CATENA* **2023**, *226*, 107068. [CrossRef]

16. Tang, C.S.; Cheng, Q.; Leng, T.; Shi, B.; Zeng, H.; Inyang, H.I. Effects of wetting-drying cycles and desiccation cracks on mechanical behavior of an unsaturated soil. *CATENA* **2020**, *194*, 104721. [CrossRef]

17. Cheng, Q.; Tang, C.S.; Xu, D.; Zeng, H.; Shi, B. Water infiltration in a cracked soil considering effect of drying-wetting cycles. *J. Hydrol.* **2021**, *593*, 125640. [CrossRef]

18. Zhao, B.; Santamarina, J.C. Desiccation crack formation beneath the surface. *Géotechnique* **2020**, *70*, 181–186. [CrossRef]

19. Julina, M.; Thyagaraj, T. Combined effects of wet-dry cycles and interacting fluid on desiccation cracks and hydraulic conductivity of compacted clay. *Eng. Geol.* **2020**, *267*, 105505. [CrossRef]

20. Rayhani, M.H.; Yanful, E.K.; Fakher, A. Desiccation-induced cracking and its effect on the hydraulic conductivity of clayey soils from Iran. *Can. Geotech. J.* **2007**, *44*, 276–283. [CrossRef]

21. Zhang, G.; Wang, R.; Qian, J.Y.; Zhang, J.M.; Qian, J.G. Effect study of cracks on behavior of soil slope under rainfall conditions. *Soils Found.* **2012**, *52*, 634–643. [CrossRef]

22. Xue, Q.; Larose, E.; Moreau, L.; Thery, R.; Abraham, O.; Henault, J.M. Ultrasonic monitoring of stress and cracks of the 1/3 scale mock-up of nuclear reactor concrete containment structure. *Struct. Health Monit.* **2022**, *21*, 1474–1482. [CrossRef]

23. Zhang, Z.; Fu, X.; Sheng, Q.; Du, Y.; Zhou, Y.; Huang, J. Stability of cracking deposit slope considering parameter deterioration subjected to rainfall. *Int. J. Geomech.* **2021**, *21*, 05021001. [CrossRef]

24. Pellegrini, S.; García, G.; Peñas-Castejon, J.M.; Vignozzi, N.; Costantini, E.A. Pedogenesis in mine tails affects macroporosity, hydrological properties, and pollutant flow. *CATENA* **2016**, *136*, 3–16. [CrossRef]

25. Tang, C.S.; Cui, Y.J.; Tang, A.M.; Shi, B. Experiment evidence on the temperature dependence of desiccation cracking behavior of clayey soils. *Eng. Geol.* **2010**, *114*, 261–266. [CrossRef]

26. Tang, C.S.; Cui, Y.J.; Shi, B.; Tang, A.M.; Liu, C. Desiccation and cracking behaviour of clay layer from slurry state under wetting–drying cycles. *Geoderma* **2011**, *166*, 111–118. [CrossRef]

27. Zeng, H.; Tang, C.S.; Zhu, C.; Vahedifard, F.; Cheng, Q.; Shi, B. Desiccation cracking of soil subjected to different environmental relative humidity conditions. *Eng. Geol.* **2022**, *297*, 106536. [CrossRef]

28. Kumar, H.; Huang, S.; Mei, G.; Garg, A. Influence of feedstock type and particle size on efficiency of biochar in improving tensile crack resistance and shear strength in lean clayey soil. *Int. J. Damage Mech.* **2021**, *30*, 646–661. [CrossRef]

29. Lakshmikantha, M.R.; Prat, P.C.; Ledesma, A. Experimental evidence of size effect in soil cracking. *Can. Geotech. J.* **2012**, *49*, 264–284. [CrossRef]

30. Kishné, A.S.; Morgan, C.L.; Ge, Y.; Miller, W.L. Antecedent soil moisture affecting surface cracking of a Vertisol in field conditions. *Geoderma* **2010**, *157*, 109–117. [CrossRef]

31. Zeng, H.; Tang, C.S.; Cheng, Q.; Inyang, H.I.; Rong, D.Z.; Lin, L.; Shi, B. Coupling effects of interfacial friction and layer thickness on soil desiccation cracking behavior. *Eng. Geol.* **2019**, *260*, 105220. [CrossRef]

32. Zeng, H.; Tang, C.S.; Cheng, Q.; Zhu, C.; Yin, L.Y.; Shi, B. Drought-induced soil desiccation cracking behavior with consideration of basal friction and layer thickness. *Water Resour. Res.* **2020**, *56*, e2019WR026948. [CrossRef]

33. Sánchez, M.; Manzoli, O.L.; Guimarães, L.J. Modeling 3-D desiccation soil crack networks using a mesh fragmentation technique. *Comput. Geotech.* **2014**, *62*, 27–39. [CrossRef]

34. Chertkov, V.Y. Shrinkage anisotropy characteristics from soil structure and initial sample/layer size. *Geoderma* **2013**, *200–201*, 1–8. [CrossRef]

35. Tang, C.; Shi, B.; Liu, C.; Zhao, L.; Wang, B. Influencing factors of geometrical structure of surface shrinkage cracks in clayey soils. *Eng. Geol.* **2008**, *101*, 204–217. [CrossRef]

36. Gui, Y.L.; Zhao, Z.Y.; Kodikara, J.; Bui, H.H.; Yang, S.Q. Numerical modelling of laboratory soil desiccation cracking using UDEC with a mix-mode cohesive fracture model. *Eng. Geol.* **2016**, *202*, 14–23. [CrossRef]

37. Li, J.H.; Li, L.; Chen, R.; Li, D.Q. Cracking and vertical preferential flow through landfill clay liners. *Eng. Geol.* **2016**, *206*, 33–41. [CrossRef]

38. Yuan, S.; Yang, B.; Liu, J.; Cao, B. Influence of fibers on desiccation cracks in sodic soil. *Bull. Eng. Geol. Environ.* **2021**, *80*, 3207–3216. [CrossRef]

39. Cheng, Q.; Tang, C.S.; Zhu, C.; Li, K.; Shi, B. Drying-induced soil shrinkage and desiccation cracking monitoring with distributed optical fiber sensing technique. *Bull. Eng. Geol. Environ.* **2020**, *79*, 3959–3970. [CrossRef]

40. Zhang, H.H.; Liu, Z.B.; Ma, X.F.; Zhang, H.J.; Qian, J.G. Monitoring of early curing stage of cemented soil using polymer optical fiber sensors and microscopic observation. *Constr. Build. Mater.* **2024**, *436*, 136888. [CrossRef]

41. Horpibulsuk, S.; Rachan, R.; Chinkulkijniwat, A.; Raksachon, Y.; Suddeepong, A. Analysis of strength development in cement-stabilized silty clay from microstructural considerations. *Constr. Build. Mater.* **2010**, *24*, 2011–2021. [CrossRef]

42. Ata, A.A.; Salem, T.N.; Elkhawas, N.M. Properties of soil–bentonite–cement bypass mixture for cutoff walls. *Constr. Build. Mater.* **2015**, *93*, 950–956. [CrossRef]

43. He, K.; Deng, Y.E.; Cao, Z.Q.; Zhang, X.F. Engineering performance and microscale structure of activated high titanium slag-soil-cement-bentonite (HTS-SCB) slurry backfill. *Constr. Build. Mater.* **2023**, *373*, 130776. [CrossRef]

44. *GB/T 50123-2019*; Standard for Geotechnical Testing Method. China Planning Press: Beijing, China, 2019.

45. Zeng, H.; Tang, C.S.; Fraccica, A.; Zhu, C.; Tian, B.G.; Shi, B. Multi-scale investigation on dynamic characteristics of clayey soil evaporation and cracking. *Comput. Geotech.* **2024**, *171*, 106312. [CrossRef]

46. Jennings, H.M. A model for the microstructure of calcium silicate hydrate in cement paste. *Cem. Concr. Res.* **2000**, *30*, 101–116. [CrossRef]

47. Pellenq, R.M.; Lequeux, N.; Van Damme, H. Engineering the bonding scheme in C–S–H: The iono-covalent framework. *Cem. Concr. Res.* **2008**, *38*, 159–174. [CrossRef]

48. Bee, S.L.; Abdullah, M.A.; Bee, S.T.; Sin, L.T.; Rahmat, A.R. Polymer nanocomposites based on silylated-montmorillonite: A review. *Prog. Polym. Sci.* **2018**, *85*, 57–82. [CrossRef]

49. Liu, C.L.; Tang, C.S.; Li, H.D.; Sun, K.Q.; Shi, B. Experimental study on effect of interfacial roughness on desiccation cracking behavior of soil. *J. Eng. Geol.* **2017**, *25*, 1314–1321.

50. Huang, K.; Fang, Z.; Cai, G.; Shi, X.; Huang, K.; He, Y.; Duan, W.; Tian, N. Macro and microscopic characteristics of soft soil stabilized by Portland cement-soda residue under dry-wet cycling. *Constr. Build. Mater.* **2024**, *428*, 136347. [CrossRef]

51. Hargis, C.W.; Kirchheim, A.P.; Monteiro, P.J.; Gartner, E.M. Early age hydration of calcium sulfoaluminate (synthetic ye'elimite, C_4A_3S) in the presence of gypsum and varying amounts of calcium hydroxide. *Cem. Concr. Res.* **2013**, *48*, 105–115. [CrossRef]